Theoretical Investigation of Solvent Effects on the Hydrodeoxygenation of Propionic Acid over a Ni (111) Catalyst Model

Mehdi Zare, Rajadurai Vijay Solomon, Wenqiang Yang, Adam Yonge, and Andreas Heyden*

Department of Chemical Engineering, University of South Carolina, 301 Main Street, Columbia, South Carolina 29208, USA

Abstract

The effect of two solvents, liquid water and 1,4-dioxane, has been studied from first principles on the hydrodeoxygenation of propionic acid over a Ni (111) catalyst surface model. A mean-field microkinetic model was developed to investigate these effects at a temperature of 473 K. Under all reaction conditions, a decarbonylation mechanism is favored significantly over a decarboxylation pathway. Although no significant solvent effects were observed on the decarbonylation rate, a substantial solvent stabilization of two key surface intermediates in the decarboxylation mechanism, CH_3CCOO and CH_3CHCOO, lead to a notable increase of the decarboxylation rate by two orders of magnitude in liquid water and by one order of magnitude in liquid 1,4-dioxane. Furthermore, a significant solvent stabilization of the transition state of C-H bond cleavage of the α-carbon of CH_3CHCO, relative to the stabilization of the C-C bond cleavage of the α-carbon of CH_3CHCO, leads to a change in dominant pathway in the liquid phase environments. Finally, a sensitivity analysis shows that the C-OH bond cleavage of propionic acid and C-C bond cleavage of the α-carbon of CH_3CHCO are the most rate controlling states in the gas phase. In contrast, in solvents the dehydrogenation of CH_3CHCO becomes the most influential step. This shift in rate controlling state is attributed to the solvent effect on the dehydrogenation of CH_3CHCO, which is facilitated in aqueous phase. Overall, it is likely that the investigated (111) facet of Ni is not active for the hydrodeoxygenation of propionic acid in neither the gas nor liquid phase and other Ni facets or phases must be responsible for the experimentally observed kinetics.

*Corresponding author: email: heyden@cec.sc.edu

1. Introduction

A consistent increase in fossil fuel demand and global warming concerns originating from the release of carbon dioxide during fossil fuel combustion have drawn increased attention toward utilization of alternative fuel sources and technologies such as the conversion of biomass to fuels.[1] Hydrodeoxygenation (HDO) is one of the more promising routes for upgrading pyrolysis bio-oils for producing liquid transportation fuels.[2] The hydrodeoxygenation of organic acids, present in e.g. pyrolysis oils, is often found to be a rate controlling HDO process such that there is a desire to design supported transition metal catalysts that can efficiently convert the organic acids into alcohols and alkanes. The HDO catalysts must have good activity, be of low cost, and reasonably stable against coke formation. Some studies have shown Ni-based catalysts to be promising candidates for the HDO of bio-oils to fuels.[3-6] For example, Bykova et al.[3] tested a series of Ni-based catalysts with different stabilizing components for the HDO of guaiacol as a bio-oil model compound. They found Ni-based catalysts prepared by the sol-gel method and stabilized with SiO_2 and ZrO_2 are highly active, and the high activity of these catalysts correlates with nickel loading. In another study, Yin et al.[5] used a bimetallic Ni-Cu catalyst with high Ni loading (up to 50%) for catalytic hydrotreatment of fast pyrolysis liquids. Their results show a low rate of undesired gas and coke/char formation when using a high Ni loading. Similarly, in Ardiyanti et al.'s work[4] the catalyst with the highest Ni loading (58 wt % Ni) promoted with Pd (0.7 wt %) was the most active, yielding oil products with improved properties such as low oxygen content and a lower tendency for coke formation.

Another factor playing an important role in the HDO of organic acids is the solvent environment. Experimental studies use various solvents, yet how and why the solvent alters the reaction mechanism remains unknown. For example, Hoelderich et al.[7] reported that in the catalytic deoxygenation of oleic acid (C18) over Pd/C, the presence of water can change the selectivity towards C17 hydrocarbons by up to 20%. Also, Wan et al.[8] discovered that when water is replaced with *n*-heptane at otherwise similar conditions, the esterification reaction is favored over ethanol reformation/hydrogenolysis, resulting in substantial formation of ethyl acetate. Although the solvent effect in a heterogenous catalyst can qualitatively be explained by the impact of solvent polarity, more work remains to be done to explain this important effect quantitatively.

This effect can be quantified computationally using various solvation schemes such as implicit, explicit, or hybrid explicit and implicit solvation models[9-12].

In the present study, periodic DFT calculations coupled with our implicit solvation scheme for metal surfaces (iSMS)[13] are used for the investigation of the HDO of propionic acid (PAC) over a Ni(111) catalyst surface model in both vacuum and solvent environments. Decarboxylation (DCX) and decarbonylation (DCN) mechanisms are considered in the reaction network bases on our prior studies of the HDO of PAC on various transition metal surfaces.[14-18] Figure 1 displays a schematic representation of all elementary reactions investigated in this study. Next, a microkinetic reaction model was developed under various reaction conditions that permits quantification of solvent effects on turnover frequency (TOF), abundant surface intermediates, reaction orders, and apparent activation barriers. This study specifically focuses on water and 1,4-dioxane as solvents that are typically used protic and aprotic polar solvents. Finally, it is noted that the lateral interaction effect of high surface coverage species such as adsorbed hydrogen and CO are considered explicitly in our microkinetic models for all surface intermediates and transition states.

2. Methods

2.1. DFT Calculations

All calculations for the catalyst slab model were performed using the DFT implantation in the Vienna Ab Initio Simulation Package (VASP)[19-20] code. The periodic surface model was constructed using the optimized lattice constant of fcc-Ni bulk, 3.518 Å, and consists of 4 Ni layers separated by 15 Å to minimize interactions between the slab and its periodic images. Each Ni layer contained 12 Ni atoms with $(3 \times 2\sqrt{3})$ periodicity, the bottom two layers were fixed, while the top two layers, as well as the adsorbates, were relaxed.

Spin-polarized calculations have been carried out at the $4 \times 4 \times 1$ Monkhorst-Pack grid using Methfessel-Paxton smearing (σ=0.2 eV) with an energy cut off for plane waves of 400 eV and a convergence criterion of a self-consistent field (SCF) of 1.0×10^{-7} eV. The projector-augmented wave method (PAW) was utilized to describe the electron–ion interactions along with the GGA-PW91[21-22] functional for describing exchange and correlation effects in the energy calculations. Transition state (TS) structures are optimized using the NEB[23] and Dimer methods.[24-

[25] We note that all reported adsorption energies, activation barriers, and reaction energies have been zero-point corrected.

Cluster model DFT calculations in vacuum were preformed using the TURBOMOLE 7.0 program package.[26-28] The cluster models were obtained by removal of the periodic boundary conditions from the periodic slabs that were constructed from previous plane-wave (VASP) calculations. A cluster model consisting of two layers and 51 Ni atoms was initially used for all surface reactions. For adsorption reactions that are somewhat more sensitive to the size of the cluster, a 3-layer model containing 86 Ni atoms was used. A convergence test of the size of the cluster is presented in the supporting information (Fig. S1). All adsorbates and metal atoms were represented by all-electron TZVP[29-31] basis sets. The Coulomb potential was approximated with the RI-J approximation using auxiliary basis sets.[32-34] Single point energy calculations were performed with a self-consistent field (SCF) energy convergence criterion of 1.0×10^{-7} Hartree. Energy calculations for different spin states were carried out to identify the lowest energy spin state. Afterwards, COSMO calculations for the cluster models in the liquid phase were performed on the lowest energy spin state configuration at the same level of theory. The dielectric constant was set to infinity as required for the Conductor-like Screening Model for Real Solvents (COSMO-RS)[35-36] calculations. Default cavity radii as well as 10% increased and decreased cavity radii were used for the Ni atoms. We note that the cavity radius is the most important solvent parameter in COSMO-RS that can, however, not be accurately determined for Ni due to insufficient experimental data, explaining why are varied the Ni cavity radius.

2.2. Solvation scheme

Solvent effects presented in this work were investigated using the implicit solvation model for solid surfaces (iSMS) method.[13] The Gibbs free energy of an intermediate adsorbed on the surface in a liquid phase environment, $G^{liquid}_{surface+intermediate}$, is calculated as:

$$G^{liquid}_{surface+intermediate} = G^{vacuum}_{surface+intermediate} + \left(G^{liquid}_{cluster+intermediate} - E^{vacuum}_{cluster+intermediate}\right) \quad (1)$$

where $G^{vacuum}_{surface+intermediate}$ is the free energy in the absence of a solvent, computed here within the harmonic approximation using plane-wave DFT calculations for periodic slab models,

$G^{liquid}_{cluster+intermediate}$ is the free energy (without vibrational contributions) of the surface species when the surface cluster model is immersed in an implicit solvent (which is obtained by extracting selected metal atoms and removing the periodic boundary conditions). We note that $G^{liquid}_{cluster+intermediate}$ does not contain vibrational contributions of the adsorbate that are already considered in the first term. Finally, $E^{vacuum}_{cluster+intermediate}$ is the DFT energy of the same cluster in the absence of the solvent. To compute the $G^{liquid}_{cluster+intermediate}$ term, COSMO-RS calculations are performed using the COSMOtherm program.[37] The COSMOtherm program for solvent thermodynamic properties requires COSMO calculations to be performed at the BP-TZVP level of theory. In addition to implicit solvation calculations performed with the iSMS method, implicit solvation calculations were also performed at 473 K using VASPsol[38-39] with a relative permittivity of water of 34.82 at reaction conditions.[40] We used the default values for the cutoff charge density, n_C, and for the width of the diffuse cavity, σ.[38] We also employed the default effective surface tension parameter, τ, for describing the cavitation, dispersion, and repulsive interaction between the solute and the solvent that are not captured by the electrostatic terms.[38] While the surface tension parameter is likely most accurate only for simulations at 298 K and not at 473 K, it is an optimized parameter of the solvent model that cannot easily be obtained at other temperatures. Due to the absence of a large number of experimental solvation data at 473 K, we decided that the default parameter is likely the most meaningful choice. All other computational details for periodic implicit solvation calculations were kept the same as in our periodic vapor phase calculations. We note that we used a reaction temperature of 473 K in this study since it is a typical reaction temperature for the HDO of organic acids[41-42].

2.3. Microkinetic modeling

For surface reactions, the forward rate constant (k_{for}) of each reaction was calculated as:

$$k_{for} = \frac{k_B T}{h} e^{\frac{-\Delta G^{\ddagger}}{k_B T}} \quad (2)$$

where k_B is the Boltzmann constant, T represents the reaction temperature, h is the Planck constant, and $\Delta G^{\ddagger}$ denotes the activation free energy at the corresponding reaction condition. In the solvated environment, the activation free energy ($\Delta G^{\ddagger}_{solvent}$) and the reaction free energy ($\Delta G^{rxn}_{solvent}$) are calculated as:

$$\Delta G^{\ddagger}_{solvent} = \Delta G^{\ddagger}_{Gas} + [G^{TS}_{solvent} - G^{IS}_{solvent}] \quad (3)$$

$$\Delta G^{rxn}_{solvent} = \Delta G^{rxn}_{Gas} + [G^{FS}_{solvent} - G^{IS}_{solvent}] \quad (4)$$

where $G^{IS}_{solvent}$, $G^{TS}_{solvent}$, and $G^{FS}_{solvent}$ represent the solvation free energies of initial, transition, and final states, respectively, and $\Delta G^{\ddagger}_{Gas}$ and ΔG^{rxn}_{Gas} are the respective activation and reaction free energies under gas phase conditions. The reverse rate constants (k_{rev}) are calculated from the thermodynamic equilibrium constants, K.

$$k_{rev} = \frac{k_{for}}{K} \quad (5)$$

For an adsorption reaction, $A(g) + * \rightarrow A^*$, the adsorption rate is given by collision theory with a sticking coefficient of 1, independent of solvent,

$$k_{for} = \frac{1}{N_0\sqrt{2\pi m_A k_B T}} \quad (6)$$

where m_A is the molecular weight of the adsorbent A and N_0 denotes the number of sites per unit area ($1.866 \times 10^{19}\ m^{-2}$). While the use of collision theory with a sticking coefficient of 1 can be questioned, we found adsorption processes to be never rate controlling in our models such that the choice of sticking coefficient has likely no effect on the reported results. Also, Zhang et al.[43] recently showed that collision theory is a reasonable approximation for adsorption processes from a liquid as long as mass transfer limitation in the liquid are negligible.

Adsorption equilibrium constants are calculated as

$$K = e^{\frac{-\Delta G^{ads}}{k_B T}} \quad (7)$$

where ΔG^{ads} is the adsorption free energy which is obtained in the presence of a solvent as,

$$\Delta G^{ads}_{solvent} = \Delta G^{ads}_{Gas} + \left[G^{A^*}_{solvent} - G^{*}_{solvent}\right] \quad (8)$$

where ΔG^{ads}_{Gas} is the adsorption free energy in the gas phase and $G^{A^*}_{solvent}$ and $G^{*}_{solvent}$ are the solvation free energies of the adsorbent A on the surface and a clean surface immersed in the solvent, respectively. With the forward and reverse rate constant calculated, all nonlinear steady-

state reactor equations are solved simultaneously under realistic reaction conditions to compute the surface coverages and turnover frequency.

2.4. Lateral interaction effects

Preliminary results of the microkinetic model indicate that CO and H are the most abundant surface species. Hence, a method which considers the lateral interaction effects of CO and H on the stability of each adsorbed species and transition state in the microkinetic model is needed. Our proposed method contains four steps.[17, 44]

Step 1: choose a reasonable coverage of high coverage species and perform DFT calculations for all intermediates in the presence of the abundant species. We define surface coverage of an adsorbate as the ratio of the number of sites it occupies to total number of sites available on the surface. For example, 3 adsorbed H or 1 adsorbed CO on a Ni surface (12 atoms) leads to 0.25 ML surface coverage of H or CO, respectively, since H occupies 1 site while CO occupies 3 sites (see below in this section for a detailed discussion).

Step 2: compute coverage dependent adsorption energies as,

$$G_i(\theta_j) = G_i(0) + \sum_j a_{ij}\,\theta_j \tag{9}$$

where $G_i(\theta_j)$ represents the free energy of species i as a function of surface coverage of abundant species, θ_j, $G_i(0)$ is the free energy of species i on the clean surface without considering the lateral interaction effect, and a_{ij} is the correction factor of species i in the presence of the abundant species j which can be acquired from equation (9) when the coverages of all other species are equal to zero,

$$a_{ij} = \frac{G_i(\theta_j) - G_i(0)}{\theta_j} \tag{10}$$

where $G_i(\theta_j)$ is the free energy of species i in the presence of only abundant species j.

Step 3: compute analogous to equation (9) for each transition state the free energy in the presence of the high surface coverage species,

$$G_n^{TS}(\theta_j) = G_n^{TS}(0) + \sum_j a_{nj}^{TS}\,\theta_j \tag{11}$$

where superscript TS indicates the transition state, subscript n represents the reaction number and a_{nj}^{TS} is the adsorption correction factor for the lateral interaction effect of the abundant species j on the transition state of reaction number n. To avoid optimizing transition states in the presence of various adsorbates, we assumed that the transition states are affected as half the reactant and half the product state and hence, the coefficient a_{nj}^{TS} is estimated as

$$a_{nj}^{TS} = \frac{1}{2}\sum_i a_{ij}^{n} \tag{12}$$

where a_{ij}^{n} represents the adsorption correction factor for the lateral interaction effect of the abundant species j on all species participating in reaction n.

Step 4: compute coverage dependent reaction and activation free energies as follows for a generic surface reaction n: $(AB^* + * \leftrightarrow A^* + B^*)$

$$\Delta G_n^{rxn}(\theta_j) = \Delta G_n^{rxn}(0) + \sum_j \Delta a_{nj}^{rxn}\,\theta_j\,, \qquad \Delta a_{nj}^{rxn} = \left(a_{A^*j} + a_{B^*j} - a_{AB^*j} - a_{*j}\right) \tag{13}$$

$$\Delta G_n^{\ddagger}(\theta_j) = \Delta G_n^{\ddagger}(0) + \sum_j \Delta a_{nj}^{\ddagger}\,\theta_j\,, \qquad \Delta a_{nj}^{\ddagger} = \left(a_{nj}^{TS} - a_{AB^*j}\right) \tag{14}$$

and for a generic adsorption reaction: $(A(g) + * \leftrightarrow A^*)$

$$\Delta G_A^{ads}(\theta_j) = \Delta G_A^{ads}(0) + \sum_j \Delta a_{Aj}^{ads}\,\theta_j\,, \qquad \Delta a_{Aj}^{ads} = \left(a_{A^*j} - a_{*j}\right) \tag{15}$$

where $\Delta G_n^{rxn}(\theta_j)$ and $\Delta G_n^{\ddagger}(\theta_j)$ are the reaction and activation free energies of reaction n, respectively, and $\Delta G_A^{ads}(\theta_j)$ is the coverage dependent adsorption free energy of species A. Similarly, $\Delta G_n^{rxn}(0)$ and $\Delta G_n^{\ddagger}(0)$ are the reaction and activation free energies of reaction n, respectively, and $\Delta G_A^{ads}(0)$ is the adsorption free energy of species A in the dilute limit.

Specifically, preliminary microkinetic modeling results, that neglect lateral interactions, show that the most abundant surface species are CO and H. Thus, we computed the adsorption

energy of all surface species in the presence of 0.25 ML H and CO. Thus, equations 13 to 15 become:

$$\Delta G_n^{rxn}(\theta_H, \theta_{CO}) = \Delta G_n^{rxn}(0) + [\Delta a_{nH}^{rxn} \times \theta_H] + [\Delta a_{nCO}^{rxn} \times \theta_{CO}] \quad (16)$$

$$\Delta G_n^{\ddagger}(\theta_H, \theta_{CO}) = \Delta G_n^{\ddagger}(0) + \left[\Delta a_{nH}^{\ddagger} \times \theta_H\right] + \left[\Delta a_{nCO}^{\ddagger} \times \theta_{CO}\right] \quad (17)$$

$$\Delta G_A^{ads}(\theta_H, \theta_{CO}) = \Delta G_A^{ads}(0) + \left[\Delta a_{AH}^{ads} \times \theta_H\right] + \left[\Delta a_{ACO}^{ads} \times \theta_{CO}\right] \quad (18)$$

Figures S2 and S3 illustrate the correction terms for individual intermediates and transition states, respectively. We note that we use a mean-field microkinetic model in this study despite significant lateral interactions that can even be attractive, such as in the case of CO and adsorbed PAC. This attractive interaction can be rationalized by the fact that the interaction between a Lewis acid and Lewis base coadsorbed on the surface is surprisingly strong.[45] Charges on adsorbed CO and PAC, separately, on the surface, and on coadsorbed CO and PAC are presented in the supporting information (Fig. S4). Strong attractive lateral interactions can result in island formation and the mean-field approximation[46] overestimating reaction rates.

Figure S5 displays the differential zero-point corrected energy of adding an extra CO or H as a function of the number of CO or H already adsorbed on the surface. Adsorbing a fifth CO molecule on a surface containing 12 surface Ni atoms leads to a significant increase in energy such that practically only four CO molecules fit on this surface while up to 12 hydrogen atoms fit. Thus, it can be concluded that on Ni (111) CO and H occupy 3 and 1 sites, respectively. We used analogue procedures to count occupied site(s) for other surface species that are bonded through carbon atoms to the surface. Given that the assumption that CO occupies 3 instead of 1 site is uncommon, we also present in the supporting information (Tables S6 and S7) all simulation results for the case that CO occupies a single site.

3. Result and discussion

3.1.Solvent effect on the adsorption strength of surface species

Solvents influence the stability of each surface intermediate and consequently facilitate certain types of cleavages. Hence, understanding the impact of the solvent environment on each individual intermediate could shed light on how a solvent could reshape the reaction mechanism.

The change in the adsorption strength of different intermediates can be quantified by considering the adsorption processes in the absence and presence of a solvent as,

$$A(g) + * (g) \leftrightarrow A^*(g) \tag{19}$$

$$A(g) + * (liq) \leftrightarrow A^*(liq) \tag{20}$$

$$\begin{aligned} \Delta\Delta(G_{ads,A}(liq)) &= \Delta G_{ads,A}(liq) - \Delta G_{ads,A}(g) \\ &= [G^{A*}(liq) - G^{A*}(g)] - [G^*(liq) - G^*(g)] \end{aligned} \tag{21}$$

where, $\Delta G_{ads,A}(liq)$ and $\Delta G_{ads,A}(g)$ are the adsorption free energies of a "gas" molecule A in the liquid (or solvent) and in the vacuum, respectively. $G^{A*}(liq)$ and $G^{A*}(g)$ are the free energies of A adsorbed on the surface in liquid and in vacuum, respectively, and $G^*(liq)$ and $G^*(g)$ are the free energies of the clean surface in liquid and in vacuum environments, respectively.

Table 1 displays the change in the adsorption free energy of each adsorbed intermediate in the presence and absence of the solvent molecules using the iSMS method. The most stabilized adsorbed intermediates are CH_3CCOO and CH_3CHCOO. In water, their adsorption strengths are increased by 0.55 and 0.31 eV, respectively, due to adsorption through the carbon atom and the charged carboxyl group pointing in the direction of the solvent. This trend can also be seen in the presence of 1,4-dioxane with a slightly lower stabilization of 0.33 eV for CH_3CCOO and 0.17 eV for CH_3CHCOO.

In general, the solvent effect on the adsorption strength is pertinent to the strength of attractive solvent-solvent interactions in solution (via e.g. hydrogen bonding in the aqueous phase) relative to attractive solvent-adsorbate interaction. In the case of adsorbed CH_3CCOO and CH_3CHCOO moieties in water, the negatively charged carboxyl group has a strong electrostatic interaction with water molecules that accounts for the stabilization of these adsorbed species in aqueous phase. Their reduced stabilization in 1,4-dixane is ascribed to the fact that 1,4-dioxane is a non-polar solvent and hence incapable of strong interaction with the charged carboxyl group.

Moreover, Table S1 shows the aqueous phase effect on the adsorption energy of intermediates at two different temperatures of 298 K and 473 K based on two implicit solvation schemes: iSMS and VASPsol. The choice of room temperature is due to the fact that all VASPsol parameters have been optimized based on experimental result at room temperature. This means VASPsol results

are most accurate at room temperature. The only parameter adjusted in the VASPsol calculations at 473 K is the relative permittivity of water. The data suggest that both iSMS and VASPsol predict (de)stabilization of adsorbed moieties qualitatively similar.

3.2.Solvent effect on elementary surface reactions

By changing the stability of various surface intermediates and transition states, the solvent environment plays an important role in altering the overall reaction pathway. Therefore, to elucidate the solvent effect on each elementary reaction, the reaction and activation free energies of all elementary steps in vacuum and in solvents are computed at 473 K using our iSMS method (see Table 2).

Propionic acid is consumed directly through three main reactions, which produce three different intermediates: propanoyl (CH_3CH_2CO) as the product of OH removal of PAC in step 1 ($\Delta(\Delta G_{rxn}^{water}) = 0.00$,$\Delta\left(\Delta G_{rxn}^{1,4-dioxane}\right) = 0.03$), $CH_3CHCOOH$ as the product of dehydrogenation of the α-carbon of PAC in step 2 ($\Delta(\Delta G_{rxn}^{water}) = -0.07$, $\Delta\left(\Delta G_{rxn}^{1,4-dioxane}\right) = -0.03$), and propionate ($CH_3CH_2COO$) as the product of O-H bond dissociation of PAC in step 28 ($\Delta(\Delta G_{rxn}^{water}) = -0.03$, $\Delta\left(\Delta G_{rxn}^{1,4-dioxane}\right) = 0.00$). Based on the solvent effect values on the reaction and activation free energies of these three paths, it appears that the solvents do not impact the starting reactions of HDO of propionic acid notably.

Furthermore, Table 2 illustrates a small change in the reaction and activation free energies of decarbonylation steps in the presence of liquid water or 1,4-dioxane. For decarbonylation steps that produce CO, the reaction energies in water and 1,4-dioxane are around 0.1 eV more exergonic than in the gas phase as a result of CO adsorption being stabilized in water and 1,4-dioxane by 0.25 and 0.18 eV, respectively (Table 1). In contrast to the small effect of the liquid phase environments on the DCN reactions, the solvent effect is pronounced on the elementary reactions of the DCX. For convenience of comparison of the solvent effect on important elementary reaction steps of the DCX, we classified them into three different classes of similar types of bond dissociations.

Class I: *α-carbon dehydrogenation*. The solvent effect on the reaction and activation free energies of dehydrogenation of CH_3CH_2COO in step 30 is -0.27 and -0.17 eV in water and -0.14 and -0.09 eV in 1,4-dioxane, respectively. A slightly higher exergonic solvent effect in water compared to in 1,4-dioxane originates from its polarity that in turn stabilizes CH_3CHCOO adsorption (the main product of this step) more in water than in 1,4-dioxane. Another important dehydrogenation reaction occurs in step 34, where CH_3CHCOO, the second most stabilized intermediate in the liquid phases, is converted to CH_3CCOO, the most stabilized intermediate in the presence of the solvents. In particular, a decline of 0.26 eV in the reaction free energy in water turns the endergonic reaction in vacuum into an exergonic reaction in aqueous phase which facilitates the reaction thermodynamically. In contrast, the endergonic solvent effect on the activation barrier of this step by 0.12 and 0.09 eV in water and 1,4-dioxane, respectively, makes this reaction kinetically unfavorable in the presence of solvents.

Class II: *O-H bond cleavage:* The O-H bond dissociation of $CH_3CHCOOH$ to produce CH_3CHCOO in step 31 and CH_3CCOOH to generate CH_3CCOO in step 35 are facilitated remarkably in the presence of solvents as a result of significant stabilization of CH_3CHCOO and CH_3CCOO on the surface.

Class III: *C-C bond cleavage to produce CO_2*: Production of CH_3CH and CO_2 by C-C bond cleavage of CH_3CHCOO (step 33) and formation of CH_3C and CO_2 from CH_3CCOO (step 38) are some of the most influenced DCX elementary reactions by a liquid phase environment. The solvents have endergonic effects on the reaction and activation free energies of these steps since the reactant states of these steps (CH_3CHCOO and CH_3CCOO) are stabilized significantly compared to the corresponding products and TS of these steps in the presence of the solvent molecules.

Overall, both solvents altered the elementary reactions in the DCX mechanism significantly while the solvent effect is small on the elementary reaction steps in the DCN mechanism. In addition, the same calculations were performed using the VASPsol program package and the results are compared to iSMS in Table S3 and S4 at 298 K and 473K. In the case of the above-mentioned O-H bond cleavage reactions (step 31 and step 35), VASPsol predicts endergonic solvent effects on activation barriers which contradicts both our iSMS results and our intuition and experimental studies.[47-53]

3.3. Microkinetic modeling

To predict the overall TOF of our reaction network in both the presence and absence of a solvent, a microkinetic model at a temperature of 473 K was developed. H_2 and CO partial pressures were set to 0.1 and 0.001 bar, respectively, and the partial pressure of propionic acid, H_2O (in the absence of liquid water), and CO_2 were set to 1 bar. In liquid water, the water chemical potential and partial pressure were computed assuming equilibrium between the liquid and a gas phase, i.e.

$$x_{H_2O} f^L_{H_2O} = y_{H_2O} P_{tot} = P_{H_2O} \quad (22)$$

where x_{H_2O} is the mole fraction of water in the liquid phase (assumed to be close to 1), $f^L_{H_2O}$ is the pure water fugacity at 473 K, y_{H_2O} is the water mole fraction in the vapor phase, P_{tot} is the total pressure of the system, and P_{H_2O} indicates the water partial pressure assuming an ideal gas phase. The pure water fugacity at 473 K was obtained from a steam table and a Lee/Kesler generalized-correlation table,[54] the partial pressure of water was calculated to be 14.36 bar and this value was used in all liquid water microkinetic models. In the following sections, we represent our microkinetic results both in the gas phase and in the solvent environments and clarify the solvent influence on important parameters of the reaction network.

3.3.1. Dominant pathways and TOF

To determine the surface coverage, rate of each elementary surface reaction, and the overall turnover frequency (defined here as the consumption of propionic acid), a microkinetic model was developed taking the lateral interaction effects of the most dominant surface species, CO and H, into account in both the gas phase and condensed phase models. Table 3 summarizes the overall TOF, the decarboxylation and decarbonylation rate, and the dominant species coverages during the HDO of propionic acid over the Ni (111) catalyst surface in various reaction environments. In addition, the TOF of each individual elementary reaction is listed in Table 4. Next, the dependence of the overall vapor phase TOF on CO and H_2 partial pressures is provided in Table S5. Finally, Figure 2 exhibits a schematic of the dominant pathways in the gas and liquid phase environments.

3.3.1.1. Gas phase

The microkinetic model predicts that the dominant pathway begins with the removal of the hydroxyl group of propionic acid in step 1, followed by dehydrogenation of the α-carbon of propanoyl in step 4, decarbonylation of CH_3CHCO in step 8, hydrogenation of CH_3CH in step 25, and finally dehydrogenation of the β-carbon in step 27 to produce ethylene. The most abundant species on the surface are H and CO with coverages of 0.631 and 0.357, respectively. Moreover, the free site coverage is 0.011. The overall TOF, which includes both DCX and DCN, is determined to be $3.46 \times 10^{-8}\ s^{-1}$. The decarbonylation rate is $3.46 \times 10^{-8}\ s^{-1}$, while the decarboxylation rate is predicted to be $8.72 \times 10^{-13}\ s^{-1}$. Hence, the selectivity towards DCN is close to 100% in the vapor phase. We note that an experimental study of catalytic HDO of propionic acid over supported group VIII noble metals performed by Lugo-Jose et al.[55] found a TOF of $1.5 \times 10^{-4}\ s^{-1}$ over a Ni/SiO_2 catalyst at 473 K. Therefore, it is possible that the investigated (111) facet of Ni is not the most relevant active site for this catalytic transformation and other Ni facets or phases could be responsible for the experimentally observed kinetics.

3.3.1.2. Liquid water and 1,4-dioxane

The dominant pathway in the liquid phases is the same as in the gas phase until CH_3CHCO formation. Then, the dominant pathway follows a dehydrogenation in step 9 to form the CH_3CCO intermediate, a C-C bond cleavage in step 14 to produce CH_3C, and further hydrogenations through steps 24, 25, and the dehydrogenation of the β-carbon from CH_3CH_2 in step 27 to produce ethylene. This shift in the dominant pathway is attributed to the activation barriers of C-C bond dissociation of CH_3CHCO (step 8) and C-H bond cleavage of the α-carbon of CH_3CHCO (step 9), which are 0.15 and 0.19 eV, respectively, in the gas phase. We conclude that due to the lower activation barrier of step 8 relative to step 9, step 8 is preferred in the gas phase. On the other hand, the activation barrier of step 8 is barely changed in the condensed phases while that of step 9 is decreased by 0.06 and 0.03 eV in water and 1,4-dioxane, respectively. Consequently, step 9 is more favorable in the condensed phases and hence forces the catalytic pathway toward the production of CH_3CHCO rather than CH_3CH. As shown in Table 4, the overall TOF in the liquid phases is very similar to the one in the gas phase and does not strongly depend on the cavity radius of Ni. However, the abundant adsorbed intermediates change in liquid phase. The CO coverage increases while the hydrogen coverage significantly decreases. Furthermore, the free site coverage decreases in the presence of the liquid phase. The overall effect on the turnover frequency is not

significant since the decarbonylation pathway is the dominant HDO pathway and it is not strongly affected by the solvent. In contrast, the DCX pathways are more affected by liquid water and the DCX rate is increased by approximately two orders of magnitude in liquid water and one order of magnitude in liquid 1,4-dioxane.

3.3.2. Sensitivity analysis, apparent activation barrier, and reaction orders

To analyze the sensitivity of each individual elementary reaction, we used Campbell's degree of rate control,[56-60] $X_{RC,i}$. This criterion describes which transition state is the most influential on the overall reaction rate.

$$X_{RC,i} = \frac{k_i}{r}\left(\frac{\partial r}{\partial k_i}\right)_{K_i, k_j \neq k_i} \tag{23}$$

where r is the overall reaction rate, k_i is the forward rate constant for step i, and K_i is the equilibrium constant for step i.

Next, the apparent activation barriers were computed in the temperature ranges of 473 to 623 K in all reaction environments.

$$E_a = RT^2\left(\frac{\partial \ln(r)}{\partial T}\right)_{p_i} \tag{24}$$

Figure 3 demonstrates the overall TOF as a function of inverse temperature in different reaction environments at a hydrogen partial pressure of 0.1 bar.

Finally, the reaction order with respect to hydrogen, CO and propionic acid were calculated at 473 K and a pressure ranges of 0.9 to 1.1 bar for H_2, 7.5×10^{-4} to 12.5×10^{-4} bar for CO, and 0.9 to 1.1 bar for PAC.

$$a_i = \left(\frac{\partial \ln(r)}{\partial \ln(p_i)}\right)_{T, p_{j \neq i}} \tag{25}$$

3.3.2.1.Gas phase

At 473 K, microkinetic modeling results suggest that the initial C-OH bond dissociation in step 1 is the most sensitive transition state in the gas phase with an X_{RC} value of 0.65. Another sensitive transition state belongs to step 8 (C-C bond cleavage of α-carbon of CH_3CHCO), $X_{RC} =$

0.26. Also, step 9 (C-H bond cleavage of α-carbon of CH_3CHCO) with $X_{RC} = 0.03$ is the third most important step given that step 8 and 9 are two competing steps in the reaction network. Finally, the apparent activation energy is predicted to be 2.38 eV and the reaction rate is independent of CO partial pressure ($a_{CO} = 0$), drops almost with a negative square of the hydrogen partial pressure ($a_{H_2} = -2.2$), and increases linearly with propionic acid partial pressure ($a_{PAC} = 1.0$).

3.3.2.2.Liquid water

The overall turnover frequency is highly sensitive to the reaction barrier of steps 9 (dehydrogenation of α-carbon of CH_3CHCO) in liquid water. This is attributed to the shift in the dominant pathway leading to step 9 becoming more favorable in the condensed phase. The values of Campbell's degree of rate control are 0.88 for step 9, 0.10 for step 1, and 0.01 for step 8. The apparent activation energy obtained from the microkinetic model is 2.71 eV. In contrast to the gas phase, the reaction rate decreases with CO partial pressure ($a_{CO} = -0.7$) in water. The reaction orders with respect to hydrogen and PAC remain approximately the same as those in the gas phase ($a_{H_2} = -1.4, a_{PAC} = 1.0$).

3.3.2.3.Liquid 1,4-dioxane

In liquid 1,4-dioxane, at 473 K, steps 9 and 1 are the most sensitive transition states with $X_{RC} = 0.55$ and $X_{RC} = 0.39$, respectively, and step 8 has $X_{RC} = 0.03$. The decrease in X_{RC} from 0.88 in water to 0.55 in 1,4-dioxane is related to a stronger stabilization of the transition state of step 9 in liquid water compared to that in 1,4-dioxane. The apparent activation barrier is 2.44 eV in the presence of 1,4-dioxane and the reaction orders are almost similar to those in the liquid water environment ($a_{CO} = -0.4$ $a_{H_2} = -1.7, a_{PAC} = 1.0$).

3.3.3. Comparison of implicit solvation models

While we have more confidence in our iSMS solvation model relative to VASPsol, we also solved the microkinetic model using free energies computed with VASPsol in (implicit) liquid water at 473 K. Table S11 in the supporting information provides a detailed comparison between these two different solvent models. Overall, both solvation schemes predict a similar solvent effect on the decarbonylation and decarboxylation of PAC. The overall rate and the DCN rate are

decreased in liquid water over Ni(111) while the DCX rate is increased. While iSMS predicts a decrease of ~80% relative to the vapor phase for the DCN rate, VASPsol only predicts a decrease of ~50%. Next, iSMS predicts an increase in DCX rate by a factor 17 relative to the vapor phase, while VASPsol predicts an increase by a factor 142. Nevertheless, the DCX hardly contributes to the overall rate in both solvation schemes. The key differences between the solvation models are the surface coverages of CO and H and a change in the rate controlling step being predicted by the different solvation models. iSMS predicts a stronger solvent stabilization of CO on the surface of 0.25 eV relative to a stabilization of only 0.08 eV predicted by VASPsol (see Table S1), explaining the difference in surface coverage. Next, iSMS predicts the C-H bond cleavage of CH_3CHCO in step 9 to be the rate determining step in aqueous phase, while VASPsol predicts the C-C bond cleavage of CH_3CHCO in step 8 to be the rate determining step. This difference in rate controlling step is a result of the opposite solvent effect predicted with iSMS and VASPsol on the activation barrier of step 9 ($\Delta\Delta G_{iSMS}^{act} = -0.06\ eV, \Delta\Delta G_{VASPsol}^{act} = 0.07\ eV$, see Table S4). We note here that all iSMS calculations with different cavity radius for Ni predict a solvent stabilization in water, leading us to have more confidence in the iSMS calculations (see Table S10).

4. Conclusion

A microkinetic model has been developed for the decarboxylation and decarbonylation of propanoic acid over Ni(111) that considers the lateral interaction effect of the most dominant surface species, CO and H. In addition, the effect of two solvents, liquid water and 1,4-dioxane, has been investigated with the help of periodic DFT calculations, implicit solvation scheme, and microkinetic modeling. Mean-field microkinetic models were developed for each solvent at a temperature of 473 K and a hydrogen partial pressure of 0.1 bar. Under all conditions, the decarbonylation is favored over the decarboxylation. The dominant pathway in gas phase begins with the removal of the hydroxyl group of propionic acid in step 1 (C-OH bond cleavage), followed by two dehydrogenations and one hydrogenation steps to produce ethylene, i.e., $CH_3CH_2COOH \rightarrow CH_3CH_2CO \rightarrow CH_3CHCO \rightarrow CH_3CH \rightarrow CH_3CH_2 \rightarrow CH_2CH_2$. Next, the dominant pathway in the condensed phases shifts after production of CH_3CHCO. It continues with a dehydrogenation step to form a CH_3CCO surface intermediate, followed by decarbonylation to produce CH_3C, and subsequent hydrogenations and one last dehydrogenation to reach ethylene, i.e., CH_3CH_2COOH

→ CH_3CH_2CO → CH_3CHCO → CH_3CCO → CH_3C → CH_3CH → CH_3CH_2 → CH_2CH_2. In the presence of a significant hydrogen pressure, ethylene can be hydrogenated to ethane.

Although no significant solvent effect was observed on the decarbonylation rate, liquid water and 1,4-dioxane increase the decarboxylation rate by two orders of magnitude and one order of magnitude, respectively, relative to the gas phase. This noticeable solvent effect on the decarboxylation rate can be explained by the significant solvent stabilization of two key surface intermediates in the decarboxylation mechanism, CH_3CCOO and CH_3CHCOO. Next, a sensitivity analysis shows that C-OH bond cleavage of propionic acid is the most rate controlling step in the gas phase ($X_{RC1} = 0.65$), In solvent environments, its dominance will be replaced with reaction step 9 (C-H bond cleavage of α-carbon of CH_3CHCO). Finally, computations suggest that the (111) surface of Ni is likely not the active facet for the HDO of propionic acid neither in gas phase nor the studied solvents, and therefore other facets need to be investigated to identify the experimentally relevant active site.

Associated Content

Supporting Information

Solvent effect results at 298 and 473 K computed by VASPsol and iSMS on each species and transition state structure in the reaction network, on reaction free energies, and on activation barriers are provided. In addition, the MKM results in the gas phase at different CO and hydrogen partial pressures is included. Furthermore, a detailed comparison between iSMS and VASPsol models in predicting important reaction parameters is provided. Also shown are a convergence plot of our solvent cluster model, the CO and H lateral interaction coefficients for various surface intermediates, a charge analysis to compare separate adsorption of CO and PAC with their coadsorbed state, a differential zero-point corrected energy plot for adding an extra CO or H as a function of number of CO or H already adsorbed on the surface , respectively, are provided.

Declaration of Competing Interest

The authors declare that they have no known competing financial interests or personal relationships that could have appeared to influence the work reported in this paper.

Acknowledgements

We gratefully acknowledge financial support from the U.S. Department of Energy, Office of Basic Energy Science, Catalysis Science program under Award DE-SC0007167. In addition, this work was partially supported by the South Carolina Smart State Center for Strategic Approaches to the Generation of Electricity (SAGE). Computational resources have been provided by the National Energy Research Scientific Computing Center (NERSC) which is supported by the Office of Science of the U.S. Department of Energy and in part by XSEDE under grant number TG-CTS090100. Computational resources from the CASCADE cluster from the Environmental Molecular Sciences Laboratory (EMSL) under Pacific Northwest National Laboratory (PNNL) are also used for selected DFT calculations. Finally, computing resources from the USC High Performance Computing Group are gratefully acknowledged.

References

1. Simonetti, D. A.; Dumesic, J. A., Catalytic Production of Liquid Fuels from Biomass‐Derived Oxygenated Hydrocarbons: Catalytic Coupling at Multiple Length Scales. *Catalysis Reviews* **2009,** *51* (3), 441-484.
2. He, Z.; Wang, X., Hydrodeoxygenation of model compounds and catalytic systems for pyrolysis bio-oils upgrading. *Catalysis for Sustainable Energy* **2012,** *1*, 28-52.
3. Bykova, M. V.; Ermakov, D. Y.; Kaichev, V. V.; Bulavchenko, O. A.; Saraev, A. A.; Lebedev, M. Y.; Yakovlev, V. A., Ni-based sol–gel catalysts as promising systems for crude bio-oil upgrading: Guaiacol hydrodeoxygenation study. *Applied Catalysis B: Environmental* **2012,** *113-114*, 296-307.
4. Ardiyanti, A. R.; Bykova, M. V.; Khromova, S. A.; Yin, W.; Venderbosch, R. H.; Yakovlev, V. A.; Heeres, H. J., Ni-Based Catalysts for the Hydrotreatment of Fast Pyrolysis Oil. *Energy & Fuels* **2016,** *30* (3), 1544-1554.
5. Yin, W.; Kloekhorst, A.; Venderbosch, R. H.; Bykova, M. V.; Khromova, S. A.; Yakovlev, V. A.; Heeres, H. J., Catalytic hydrotreatment of fast pyrolysis liquids in batch and continuous set-ups using a bimetallic Ni–Cu catalyst with a high metal content. *Catalysis Science & Technology* **2016,** *6* (15), 5899-5915.
6. Ardiyanti, A. R.; Khromova, S. A.; Venderbosch, R. H.; Yakovlev, V. A.; Heeres, H. J., Catalytic hydrotreatment of fast-pyrolysis oil using non-sulfided bimetallic Ni-Cu catalysts on a δ-Al2O3 support. *Applied Catalysis B: Environmental* **2012,** *117-118*, 105-117.
7. Arend, M.; Nonnen, T.; Hoelderich, W. F.; Fischer, J.; Groos, J., Catalytic deoxygenation of oleic acid in continuous gas flow for the production of diesel-like hydrocarbons. *Applied Catalysis A: General* **2011,** *399* (1), 198-204.
8. Wan, H.; Chaudhari, R. V.; Subramaniam, B., Aqueous Phase Hydrogenation of Acetic Acid and Its Promotional Effect on p-Cresol Hydrodeoxygenation. *Energy & Fuels* **2013,** *27* (1), 487-493.
9. Saleheen, M.; Verma, A. M.; Mamun, O.; Lu, J.; Heyden, A., Investigation of solvent effects on the hydrodeoxygenation of guaiacol over Ru catalysts. *Catalysis Science & Technology* **2019,** *9* (22), 6253-6273.
10. Saleheen, M.; Zare, M.; Faheem, M.; Heyden, A., Computational Investigation of Aqueous Phase Effects on the Dehydrogenation and Dehydroxylation of Polyols over Pt(111). *The Journal of Physical Chemistry C* **2019,** *123* (31), 19052-19065.
11. Car, R.; Parrinello, M., Unified Approach for Molecular Dynamics and Density-Functional Theory. *Physical Review Letters* **1985,** *55* (22), 2471-2474.
12. Carloni, P.; Rothlisberger, U.; Parrinello, M., The Role and Perspective of Ab Initio Molecular Dynamics in the Study of Biological Systems. *Accounts of Chemical Research* **2002,** *35* (6), 455-464.
13. Faheem, M.; Suthirakun, S.; Heyden, A., New Implicit Solvation Scheme for Solid Surfaces. *The Journal of Physical Chemistry C* **2012,** *116* (42), 22458-22462.
14. Lu, J.; Behtash, S.; Heyden, A., Theoretical Investigation of the Reaction Mechanism of the Decarboxylation and Decarbonylation of Propanoic Acid on Pd(111) Model Surfaces. *The Journal of Physical Chemistry C* **2012,** *116* (27), 14328-14341.
15. Behtash, S.; Lu, J.; Faheem, M.; Heyden, A., Solvent effects on the hydrodeoxygenation of propanoic acid over Pd(111) model surfaces. *Green Chemistry* **2014,** *16* (2), 605-616.
16. Lu, J.; Faheem, M.; Behtash, S.; Heyden, A., Theoretical investigation of the decarboxylation and decarbonylation mechanism of propanoic acid over a Ru(0001) model surface. *Journal of Catalysis* **2015,** *324*, 14-24.
17. Yang, W.; Solomon, R. V.; Lu, J.; Mamun, O.; Bond, J. Q.; Heyden, A., Unraveling the mechanism of the hydrodeoxygenation of propionic acid over a Pt (1 1 1) surface in vapor and liquid phases. *Journal of Catalysis* **2020,** *381*, 547-560.

18. Behtash, S.; Lu, J.; Mamun, O.; Williams, C. T.; Monnier, J. R.; Heyden, A., Solvation Effects in the Hydrodeoxygenation of Propanoic Acid over a Model Pd(211) Catalyst. *The Journal of Physical Chemistry C* **2016,** *120* (5), 2724-2736.
19. Kresse, G.; Furthmüller, J., Efficiency of ab-initio total energy calculations for metals and semiconductors using a plane-wave basis set. *Computational Materials Science* **1996,** *6* (1), 15-50.
20. Kresse, G.; Hafner, J., Ab initio molecular dynamics for liquid metals. *Physical Review B* **1993,** *47* (1), 558-561.
21. Perdew, J. P.; Wang, Y., Accurate and simple analytic representation of the electron-gas correlation energy. *Physical Review B* **1992,** *45* (23), 13244-13249.
22. Perdew, J. P.; Yue, W., Accurate and simple density functional for the electronic exchange energy: Generalized gradient approximation. *Physical Review B* **1986,** *33* (12), 8800-8802.
23. Henkelman, G.; Uberuaga, B. P.; Jónsson, H., A climbing image nudged elastic band method for finding saddle points and minimum energy paths. *The Journal of Chemical Physics* **2000,** *113* (22), 9901-9904.
24. Henkelman, G.; Jónsson, H., A dimer method for finding saddle points on high dimensional potential surfaces using only first derivatives. *The Journal of Chemical Physics* **1999,** *111* (15), 7010-7022.
25. Heyden, A.; Bell, A. T.; Keil, F. J., Efficient methods for finding transition states in chemical reactions: Comparison of improved dimer method and partitioned rational function optimization method. *The Journal of Chemical Physics* **2005,** *123* (22), 224101.
26. Ahlrichs, R.; Bär, M.; Häser, M.; Horn, H.; Kölmel, C., Electronic structure calculations on workstation computers: The program system turbomole. *Chemical Physics Letters* **1989,** *162* (3), 165-169.
27. Treutler, O.; Ahlrichs, R., Efficient molecular numerical integration schemes. *The Journal of Chemical Physics* **1995,** *102* (1), 346-354.
28. TURBOMOLE V6.0 2009, a development of University of Karlsruhe and Forschungszentrum Karlsruhe GmbH, 1989−2007, TURBOMOLE GmbH, since 2007.
29. Weigend, F., Accurate Coulomb-fitting basis sets for H to Rn. *Physical Chemistry Chemical Physics* **2006,** *8* (9), 1057-1065.
30. Weigend, F.; Ahlrichs, R., Balanced basis sets of split valence, triple zeta valence and quadruple zeta valence quality for H to Rn: Design and assessment of accuracy. *Physical Chemistry Chemical Physics* **2005,** *7* (18), 3297-3305.
31. Weigend, F.; Häser, M.; Patzelt, H.; Ahlrichs, R., RI-MP2: optimized auxiliary basis sets and demonstration of efficiency. *Chemical Physics Letters* **1998,** *294* (1), 143-152.
32. Eichkorn, K.; Treutler, O.; Öhm, H.; Häser, M.; Ahlrichs, R., Auxiliary basis sets to approximate Coulomb potentials. *Chemical Physics Letters* **1995,** *240* (4), 283-290.
33. Eichkorn, K.; Weigend, F.; Treutler, O.; Ahlrichs, R., Auxiliary basis sets for main row atoms and transition metals and their use to approximate Coulomb potentials. *Theoretical Chemistry Accounts* **1997,** *97* (1), 119-124.
34. Von Arnim, M.; Ahlrichs, R., Performance of parallel TURBOMOLE for density functional calculations. *Journal of Computational Chemistry* **1998,** *19* (15), 1746-1757.
35. Klamt, A., Conductor-like Screening Model for Real Solvents: A New Approach to the Quantitative Calculation of Solvation Phenomena. *The Journal of Physical Chemistry* **1995,** *99* (7), 2224-2235.
36. Klamt, A.; Jonas, V.; Bürger, T.; Lohrenz, J. C. W., Refinement and Parametrization of COSMO-RS. *The Journal of Physical Chemistry A* **1998,** *102* (26), 5074-5085.
37. Marsh, K. N., COSMO-RS from Quantum Chemistry to Fluid Phase Thermodynamics and Drug Design. By A. Klamt. Elsevier: Amsterdam, The Netherlands, 2005. 246 pp. $US 165. ISBN 0-444-51994-7. *Journal of Chemical & Engineering Data* **2006,** *51* (4), 1480-1480.

38. Mathew, K.; Sundararaman, R.; Letchworth-Weaver, K.; Arias, T. A.; Hennig, R. G., Implicit solvation model for density-functional study of nanocrystal surfaces and reaction pathways. *The Journal of Chemical Physics* **2014,** *140* (8), 084106.
39. Fishman, M.; Zhuang, H. L.; Mathew, K.; Dirschka, W.; Hennig, R. G., Accuracy of exchange-correlation functionals and effect of solvation on the surface energy of copper. *Physical Review B* **2013,** *87* (24), 245402.
40. Fernández, D. P.; Goodwin, A. R. H.; Lemmon, E. W.; Sengers, J. M. H. L.; Williams, R. C., A Formulation for the Static Permittivity of Water and Steam at Temperatures from 238 K to 873 K at Pressures up to 1200 MPa, Including Derivatives and Debye–Hückel Coefficients. *Journal of Physical and Chemical Reference Data* **1997,** *26* (4), 1125-1166.
41. Lugo-José, Y. K.; Monnier, J. R.; Heyden, A.; Williams, C. T., Hydrodeoxygenation of propanoic acid over silica-supported palladium: effect of metal particle size. *Catalysis Science & Technology* **2014,** *4* (11), 3909-3916.
42. Lugo-José, Y. K.; Behtash, S.; Nicholson, M.; Monnier, J. R.; Heyden, A.; Williams, C. T., Unraveling the mechanism of propanoic acid hydrodeoxygenation on palladium using deuterium kinetic isotope effects. *Journal of Molecular Catalysis A: Chemical* **2015,** *406*, 85-93.
43. Zhang, X.; Savara, A.; Getman, R. B., A Method for Obtaining Liquid–Solid Adsorption Rates from Molecular Dynamics Simulations: Applied to Methanol on Pt(111) in H2O. *Journal of Chemical Theory and Computation* **2020**.
44. Demir, B.; Kropp, T.; Rivera-Dones, K. R.; Gilcher, E. B.; Huber, G. W.; Mavrikakis, M.; Dumesic, J. A., A self-adjusting platinum surface for acetone hydrogenation. *Proceedings of the National Academy of Sciences* **2020,** *117* (7), 3446.
45. McFarland, E. W.; Metiu, H., Catalysis by Doped Oxides. *Chemical Reviews* **2013,** *113* (6), 4391-4427.
46. I. Chorkendorff, J. W. N., *Concepts of Modern Catalysis and Kinetics*. third ed.; Wiley-VCH, Weinheim: 2005.
47. Desai, S. K.; Neurock, M., First-principles study of the role of solvent in the dissociation of water over a Pt-Ru alloy. *Phys Rev B* **2003,** *68* (7), 075420:1-7.
48. Hibbitts, D. D.; Loveless, B. T.; Neurock, M.; Iglesia, E., Mechanistic Role of Water on the Rate and Selectivity of Fischer-Tropsch Synthesis on Ruthenium Catalysts. *Angew. Chem. Int. Ed. Engl.* **2013,** *52* (47), 12273-12278.
49. Zhang, X. H.; Sewell, T. E.; Glatz, B.; Sarupria, S.; Getman, R. B., On the water structure at hydrophobic interfaces and the roles of water on transition-metal catalyzed reactions: A short review. *Catal Today* **2017,** *285*, 57-64.
50. Santana, J. A.; Mateo, J. J.; Ishikawa, Y., Electrochemical Hydrogen Oxidation on Pt(110): A Combined Direct Molecular Dynamics/Density Functional Theory Study. *J Phys Chem C* **2010,** *114* (11), 4995-5002.
51. Skachkov, D.; Rao, C. V.; Ishikawa, Y., Combined First-Principles Molecular Dynamics/Density Functional Theory Study of Ammonia Electrooxidation on Pt(100) Electrode. *J Phys Chem C* **2013,** *117* (48), 25451-25466.
52. Nie, X. W.; Luo, W. J.; Janik, M. J.; Asthagiri, A., Reaction mechanisms of CO2 electrochemical reduction on Cu(111) determined with density functional theory. *J Catal* **2014,** *312*, 108-122.
53. Huang, Z. Q.; Long, B.; Chang, C. R., A theoretical study on the catalytic role of water in methanol steam reforming on PdZn(111). *Catal Sci Technol* **2015,** *5* (5), 2935-2944.
54. Smith, J. M.; Ness, H. C. V.; Abbott, M. M., *Introduction to Chemical Engineering Thermodynamics*. McGraw-Hill: New York, 2005.

55. Lugo-José, Y. K.; Monnier, J. R.; Williams, C. T., Gas-phase, catalytic hydrodeoxygenation of propanoic acid, over supported group VIII noble metals: Metal and support effects. *Applied Catalysis A: General* **2014,** *469*, 410-418.
56. Campbell, C. T., Future Directions and Industrial Perspectives Micro- and macro-kinetics: Their relationship in heterogeneous catalysis. *Topics in Catalysis* **1994,** *1* (3), 353-366.
57. Campbell, C. T., Finding the Rate-Determining Step in a Mechanism: Comparing DeDonder Relations with the "Degree of Rate Control". *Journal of Catalysis* **2001,** *204* (2), 520-524.
58. Stegelmann, C.; Andreasen, A.; Campbell, C. T., Degree of Rate Control: How Much the Energies of Intermediates and Transition States Control Rates. *Journal of the American Chemical Society* **2009,** *131* (23), 8077-8082.
59. Kozuch, S.; Shaik, S., Kinetic-Quantum Chemical Model for Catalytic Cycles: The Haber−Bosch Process and the Effect of Reagent Concentration. *The Journal of Physical Chemistry A* **2008,** *112* (26), 6032-6041.
60. Kozuch, S.; Shaik, S., A Combined Kinetic−Quantum Mechanical Model for Assessment of Catalytic Cycles: Application to Cross-Coupling and Heck Reactions. *Journal of the American Chemical Society* **2006,** *128* (10), 3355-3365.

Table 1. Solvent effect on the stability of various adsorbed species in the HDO of PAC to ethane and ethylene over a Ni(111) catalyst surface model at a reaction temperature of 473 K. $\Delta\Delta G_{rxn}$ indicates the difference in the adsorption free energy of the corresponding intermediate in the presence and the absence of the solvent. Asterisk (*) represents a surface adsorption site and multiple asterisks are indicative of the number of occupied active sites.

Adsorbed species	$\Delta\Delta G_{rxn}$, eV	
	Water	1,4-Dioxane
CH_2C***	-0.08	-0.05
CH_2CH***	-0.01	0.00
CH_2CH_2**	0.10	0.12
CH_2CHCO****	-0.09	-0.03
$CH_2CHCOOH$****	-0.11	-0.04
CH_3C***	-0.01	-0.01
CH_3CCO****	-0.12	-0.06
CH_3CCOO***	-0.55	-0.33
CH_3CCOOH***	-0.12	-0.07
CH_3CH***	0.00	-0.01
CH_3CH_2**	0.01	-0.01
CH_3CH_2CO***	-0.05	-0.04
CH_3CH_2COO**	-0.06	-0.04
CH_3CH_2COOH*	-0.03	0.02
CH_3CH_3*	0.02	0.02
CH_3CHCO**	-0.09	-0.05
CH_3CHCOO***	-0.31	-0.17
$CH_3CHCOOH$**	-0.10	-0.06
CHCH****	0.05	0.08
CHCHCO****	-0.15	-0.05
CHCHCOOH****	-0.13	-0.06
CO***	-0.25	-0.18
CO_2*	-0.04	0.01
COOH**	-0.16	-0.08
H*	-0.01	0.00
H_2O*	0.02	0.07
OH*	0.00	0.02

Table 2. Reaction and activation free energies of all elementary steps in the HDO of PAC to ethane and ethylene over a Ni(111) catalyst surface model at 473 K. $\Delta\Delta G_{rxn}$ and $\Delta\Delta G^{act}$ indicate the reaction and the activation free energy differences between corresponding reaction in the presence of solvent and in the gas phase, respectively.

#	Reaction	Vacuum		Water		1,4-Dioxane	
		ΔG_{rxn}	ΔG^{act}	$\Delta\Delta G_{rxn}$	$\Delta\Delta G^{act}$	$\Delta\Delta G_{rxn}$	$\Delta\Delta G^{act}$
0	$CH_3CH_2COOH + * \rightarrow CH_3CH_2COOH*$	0.69		-0.03		0.02	
1	$CH_3CH_2COOH* + 3* \rightarrow CH_3CH_2CO*** + OH*$	-0.25	0.60	0.00	0.00	0.03	0.00
2	$CH_3CH_2COOH* + 2* \rightarrow CH_3CHCOOH** + H*$	-0.05	0.51	-0.07	-0.03	-0.03	-0.01
3	$CH_3CH_2CO***+ 2* \rightarrow CH_3CH_2** + CO***$	-0.61	0.78	-0.14	-0.03	-0.10	0.01
4	$CH_3CH_2CO*** \rightarrow CH_3CHCO** + H*$	0.19	0.49	-0.06	-0.03	-0.02	0.00
5	$CH_3CHCOOH** + * \rightarrow CH_3CHCO** + OH*$	-0.01	0.90	0.01	-0.03	0.04	0.00
6	$CH_3CHCOOH** + 3* \rightarrow CH_2CHCOOH**** + H*$	-0.42	0.57	-0.02	0.00	0.01	0.04
7	$CH_3CHCOOH** + 2* \rightarrow CH_3CCOOH*** + H*$	-0.19	0.35	-0.03	0.00	-0.01	0.01
8	$CH_3CHCO** + 4* \rightarrow CH_3CH*** + CO***$	-1.14	0.15	-0.10	-0.01	-0.09	0.01
9	$CH_3CHCO** + 3* \rightarrow CH_3CCO**** + H*$	-0.73	0.19	-0.05	-0.06	-0.02	-0.03
10	$CH_3CHCO** + 3* \rightarrow CH_2CHCO**** + H*$	-0.43	0.49	-0.01	0.00	0.01	0.01
11	$CH_2CHCOOH**** + * \rightarrow CH_2CHCO**** + OH*$	-0.02	1.12	0.02	0.00	0.04	0.01
12	$CH_2CHCOOH**** + * \rightarrow CHCHCOOH**** + H*$	-0.14	0.47	-0.05	0.01	-0.03	0.00
13	$CH_3CCOOH*** + 2* \rightarrow CH_3CCO**** + OH*$	-0.54	0.83	-0.01	-0.08	0.03	-0.03
14	$CH_3CCO**** + 2* \rightarrow CH_3C*** +CO***$	-1.09	0.23	-0.08	-0.08	-0.08	-0.07
15	$CH_2CHCO**** + 2* \rightarrow CH_2CH*** + CO***$	-0.71	0.41	-0.11	-0.01	-0.10	0.00
16	$CH_2CHCO**** + * \rightarrow CHCHCO**** + H*$	-0.15	0.41	-0.08	0.00	-0.03	0.01
17	$CHCHCOOH**** + * \rightarrow CHCHCO**** + OH*$	-0.03	1.02	-0.01	-0.12	0.03	-0.06
18	$CHCHCO**** + 3* \rightarrow CHCH**** + CO***$	-1.37	0.21	-0.06	-0.03	-0.08	-0.02
19	$CH_2CH*** + 2* \rightarrow CHCH**** + H*$	-0.80	0.11	-0.03	0.02	-0.01	0.02
20	$CH_2CH_2** + 2* \rightarrow CH_2CH*** + H*$	-0.10	0.48	-0.06	0.01	-0.03	0.01
21	$CH_2CH*** + * \rightarrow CH_2C*** + H*$	-0.54	0.18	-0.09	-0.02	-0.06	-0.01
22	$CH_3C*** + * \rightarrow CH_2C*** + H*$	0.13	0.86	-0.08	-0.01	-0.05	0.01
23	$CH_3CH*** + * \rightarrow CH_2CH*** + H*$	0.00	0.50	-0.03	-0.03	-0.01	0.00
24	$CH_3CH*** + * \rightarrow CH_3C*** + H*$	-0.67	0.09	-0.03	0.02	-0.01	0.01
25	$CH_3CH_2** + 2* \rightarrow CH_3CH*** + H*$	-0.35	0.29	-0.03	0.01	-0.01	0.02
26	$CH_3CH_3* + 2* \rightarrow CH_3CH_2** + H*$	0.22	0.94	-0.05	-0.02	-0.03	-0.01
27	$CH_3CH_2** + * \rightarrow CH_2CH_2** + H*$	-0.25	0.16	0.01	-0.01	0.02	0.02
28	$CH_3CH_2COOH* + 2* \rightarrow CH_3CH_2COO** + H*$	-0.95	0.00	-0.03	-0.07	0.00	-0.03
29	$CH_3CH_2COO** + * \rightarrow CH_3CH_2** + CO_2*$	0.71	1.88	0.06	-0.04	0.04	-0.03
30	$CH_3CH2COO** + 2* \rightarrow CH_3CHCOO*** + H*$	0.65	1.52	-0.27	-0.17	-0.14	-0.09
31	$CH_3CHCOOH** + 2* \rightarrow CH_3CHCOO*** + H*$	-0.25	0.60	-0.23	-0.14	-0.11	-0.07
32	$CH_3CHCOOH** + 3* \rightarrow CH_3CH*** + COOH**$	-0.04	0.76	-0.06	-0.02	-0.02	0.02
33	$CH_3CHCOO*** + * \rightarrow CH_3CH*** + CO_2*$	-0.29	0.80	0.31	0.12	0.17	0.10
34	$CH_3CHCOO*** + * \rightarrow CH_3CCOO*** + H*$	0.14	0.85	-0.26	0.12	-0.17	0.09
35	$CH_3CCOOH*** + * \rightarrow CH_3CCOO*** + H*$	0.08	0.97	-0.45	-0.18	-0.27	-0.07
36	$CH_3CCOOH*** + 2* \rightarrow CH_3C*** + COOH**$	-0.53	0.57	-0.06	-0.05	-0.02	-0.02
37	$CH_2CHCOOH**** + * \rightarrow CH_2CH*** + COOH**$	0.38	0.95	-0.07	-0.01	-0.04	0.00
38	$CH_3CCOO*** + * \rightarrow CH_3C*** + CO_2*$	-1.10	0.25	0.54	0.21	0.33	0.14
39	$COOH** \rightarrow CO_2* + H*$	-0.50	0.75	0.15	-0.18	0.08	-0.14
40	$COOH** + 2* \rightarrow CO*** + OH*$	-1.11	0.34	-0.03	0.04	-0.03	0.03
41	$H_2O* + * \rightarrow OH* + H*$	-0.43	0.75	0.00	-0.01	0.00	-0.01
42	$CH_3CH_3 + * \rightarrow CH_3CH_3*$	0.81		0.02		0.02	
43	$CH_2CH_2 + 2* \rightarrow CH_2CH_2**$	0.13		0.10		0.12	
44	$H_2O + * \rightarrow H_2O*$	0.46		0.02		0.07	
45	$CO_2 + * \rightarrow CO_2*$	0.31		-0.04		0.01	
46	$CHCH + 4* \rightarrow CHCH****$	-1.86		0.05		0.08	
47	$CO + 3* \rightarrow CO***$	-0.71		-0.25		-0.18	
48	$H_2 + 2* \rightarrow H^* + H*$	-0.42		-0.01		0.00	

Table 3. Overall, decarbonylation, and decarboxylation turnover frequencies as well as important steady state surface coverages for the HDO of PAC over a Ni(111) catalyst surface model in the gas phase, and in liquid water and 1,4-dioxane at 473 K. Note that calculations for solvents were performed with the help of the COSMO-RS package with three different Ni cavity radii: with default value, with a 10% increased value and a 10% decreased value relative to the default.

Properties	**Gas**	**Water**			**1,4-Dioxane**		
		Default	*+10%*	*-10%*	*Default*	*+10%*	*-10%*
DCN TOF	3.46×10^{-08}	6.70×10^{-09}	4.07×10^{-08}	4.64×10^{-09}	1.84×10^{-08}	1.23×10^{-07}	1.15×10^{-08}
DCX TOF	8.72×10^{-13}	1.47×10^{-11}	1.47×10^{-10}	2.12×10^{-11}	5.24×10^{-13}	6.64×10^{-12}	1.02×10^{-12}
Overall TOF (s^{-1})	3.46×10^{-08}	6.71×10^{-09}	4.09×10^{-08}	4.66×10^{-09}	1.84×10^{-08}	1.23×10^{-07}	1.15×10^{-08}
θ*	0.011	0.003	0.003	0.003	0.004	0.005	0.004
θ_{H^*}	0.631	0.206	0.154	0.149	0.296	0.253	0.207
$\theta_{CO^{***}}$	0.357	0.789	0.834	0.849	0.699	0.741	0.789
$\theta_{CH3C^{***}}$	0.000	0.000	0.000	0.000	0.000	0.000	0.000
θ_{PAC^*}	0.000	0.000	0.004	0.000	0.000	0.000	0.000
$\theta_{CH3CH2COO^{**}}$	0.001	0.000	0.002	0.000	0.000	0.001	0.000

Table 4. Calculated turnover frequency (net rate) in the gas phase and in the solvents for all elementary reaction steps in the HDO of PAC over a Ni(111) catalyst model surface at a temperature of 473 K and a hydrogen partial pressure of 0.1 bar.

#	Reaction	TOF (s^{-1})		
		Gas	Water	1,4-dioxane
0	$CH_3CH_2COOH + * \rightarrow CH_3CH_2COOH*$	3.45×10^{-08}	6.69×10^{-09}	1.84×10^{-08}
1	$CH_3CH_2COOH* + 3* \rightarrow CH_3CH_2CO*** + OH*$	3.46×10^{-08}	6.70×10^{-09}	1.84×10^{-08}
2	$CH_3CH_2COOH* + 2* \rightarrow CH_3CHCOOH** + H*$	1.37×10^{-12}	8.98×10^{-12}	4.04×10^{-13}
3	$CH_3CH_2CO***+ 2* \rightarrow CH_3CH_2** + CO***$	2.65×10^{-09}	2.48×10^{-11}	2.75×10^{-10}
4	$CH_3CH_2CO*** \rightarrow CH_3CHCO** + H*$	3.19×10^{-08}	6.67×10^{-09}	1.82×10^{-08}
5	$CH_3CHCOOH** + * \rightarrow CH_3CHCO** + OH*$	5.26×10^{-13}	4.04×10^{-14}	2.85×10^{-14}
6	$CH_3CHCOOH** + 3* \rightarrow CH_2CHCOOH**** + H*$	2.47×10^{-17}	2.92×10^{-15}	2.53×10^{-16}
7	$CH_3CHCOOH** + 2* \rightarrow CH_3CCOOH*** + H*$	7.63×10^{-13}	1.24×10^{-12}	1.87×10^{-13}
8	$CH_3CHCO** + 4* \rightarrow CH_3CH*** + CO***$	2.91×10^{-08}	5.84×10^{-11}	8.26×10^{-10}
9	$CH_3CHCO** + 3* \rightarrow CH_3CCO**** + H*$	2.75×10^{-09}	6.61×10^{-09}	1.73×10^{-08}
10	$CH_3CHCO** + 3* \rightarrow CH_2CHCO**** + H*$	8.35×10^{-13}	8.27×10^{-14}	4.01×10^{-13}
11	$CH_2CHCOOH**** + * \rightarrow CH_2CHCO**** + OH*$	2.97×10^{-20}	5.83×10^{-20}	2.74×10^{-20}
12	$CH_2CHCOOH**** + * \rightarrow CHCHCOOH**** + H*$	2.21×10^{-17}	2.89×10^{-15}	2.44×10^{-16}
13	$CH_3CCOOH*** + 2* \rightarrow CH_3CCO**** + OH*$	1.62×10^{-18}	3.96×10^{-16}	1.74×10^{-17}
14	$CH_3CCO**** + 2* \rightarrow CH_3C*** + CO***$	2.75×10^{-09}	6.61×10^{-09}	1.73×10^{-08}
15	$CH_2CHCO**** + 2* \rightarrow CH_2CH*** + CO***$	2.89×10^{-16}	4.16×10^{-16}	1.58×10^{-15}
16	$CH_2CHCO**** + * \rightarrow CHCHCO**** + H*$	8.35×10^{-13}	8.23×10^{-14}	4.00×10^{-13}
17	$CHCHCOOH**** + * \rightarrow CHCHCO**** + OH*$	2.21×10^{-17}	2.89×10^{-15}	2.44×10^{-16}
18	$CHCHCO**** + 3* \rightarrow CHCH**** + CO***$	8.35×10^{-13}	8.52×10^{-14}	4.00×10^{-13}
19	$CH_2CH*** + 2* \rightarrow CHCH**** + H*$	-8.35×10^{-13}	-8.52×10^{-14}	-4.00×10^{-13}
20	$CH_2CH_2** + 2* \rightarrow CH_2CH*** + H*$	-2.40×10^{-10}	-4.76×10^{-10}	-7.02×10^{-10}
21	$CH_2CH*** + * \rightarrow CH_2C*** + H*$	-1.42×10^{-10}	-3.74×10^{-10}	-5.64×10^{-10}
22	$CH_3C*** + * \rightarrow CH_2C*** + H*$	1.42×10^{-10}	3.74×10^{-10}	5.64×10^{-10}
23	$CH_3CH*** + * \rightarrow CH_2CH*** + H*$	9.72×10^{-11}	1.03×10^{-10}	1.38×10^{-10}
24	$CH_3CH*** + * \rightarrow CH_3C*** + H*$	-2.61×10^{-09}	-6.24×10^{-09}	-1.68×10^{-08}
25	$CH_3CH_2** + 2* \rightarrow CH_3CH*** + H*$	-3.17×10^{-08}	-6.21×10^{-09}	-1.75×10^{-08}
26	$CH_3CH_3* + 2* \rightarrow CH_3CH_2** + H*$	-4.50×10^{-13}	-2.58×10^{-14}	-1.29×10^{-13}
27	$CH_3CH_2** + * \rightarrow CH_2CH_2** + H*$	3.43×10^{-08}	6.24×10^{-09}	1.77×10^{-08}
28	$CH_3CH_2COOH* + 2* \rightarrow CH_3CH_2COO** + H*$	3.73×10^{-14}	5.68×10^{-12}	1.35×10^{-13}
29	$CH_3CH_2COO** + * \rightarrow CH_3CH_2** + CO_2*$	1.23×10^{-14}	1.45×10^{-13}	2.90×10^{-14}
30	$CH_3CH2COO** + 2* \rightarrow CH_3CHCOO*** + H*$	1.81×10^{-14}	5.63×10^{-12}	1.19×10^{-13}
31	$CH_3CHCOOH** + 2* \rightarrow CH_3CHCOO*** + H*$	7.00×10^{-14}	7.70×10^{-12}	1.88×10^{-13}
32	$CH_3CHCOOH** + 3* \rightarrow CH_3CH*** + COOH**$	7.90×10^{-15}	1.00×10^{-15}	2.41×10^{-16}
33	$CH_3CHCOO*** + * \rightarrow CH_3CH*** + CO_2*$	7.52×10^{-14}	1.28×10^{-11}	2.90×10^{-13}
34	$CH_3CHCOO*** + * \rightarrow CH_3CCOO*** + H*$	1.29×10^{-14}	5.50×10^{-13}	1.76×10^{-14}
35	$CH_3CCOOH*** + * \rightarrow CH_3CCOO*** + H*$	1.06×10^{-15}	4.70×10^{-14}	7.65×10^{-16}
36	$CH_3CCOOH*** + 2* \rightarrow CH_3C*** + COOH**$	7.62×10^{-13}	1.19×10^{-12}	1.87×10^{-13}
37	$CH_2CHCOOH**** + * \rightarrow CH_2CH*** + COOH**$	2.61×10^{-18}	2.76×10^{-17}	9.43×10^{-18}
38	$CH_3CCOO*** + * \rightarrow CH_3C*** + CO_2*$	1.39×10^{-14}	5.97×10^{-13}	1.83×10^{-14}
39	$COOH** \rightarrow CO_2* + H*$	-2.18×10^{-08}	-1.03×10^{-07}	-3.22×10^{-08}
40	$COOH** + 2* \rightarrow CO*** + OH*$	2.18×10^{-08}	1.03×10^{-07}	3.22×10^{-08}
41	$H_2O* + * \rightarrow OH* + H*$	-5.63×10^{-08}	-1.10×10^{-07}	-5.07×10^{-08}
42	$CH_3CH_3 + * \rightarrow CH_3CH_3*$	-4.50×10^{-13}	-2.58×10^{-14}	-1.29×10^{-13}
43	$CH_2CH_2 + 2* \rightarrow CH_2CH_2**$	-3.46×10^{-08}	-6.71×10^{-09}	-1.84×10^{-08}
44	$H_2O + * \rightarrow H_2O*$	-5.64×10^{-08}	-1.10×10^{-07}	-5.07×10^{-08}
45	$CO_2 + * \rightarrow CO_2*$	2.18×10^{-08}	1.03×10^{-07}	3.22×10^{-08}
46	$CHCH + 4* \rightarrow CHCH****$	-5.87×10^{-23}	-6.28×10^{-24}	-2.99×10^{-23}
47	$CO + 3* \rightarrow CO***$	-5.63×10^{-08}	-1.10×10^{-07}	-5.07×10^{-08}
48	$H_2 + 2* \rightarrow H^* + H*$	2.18×10^{-08}	1.03×10^{-07}	3.22×10^{-08}

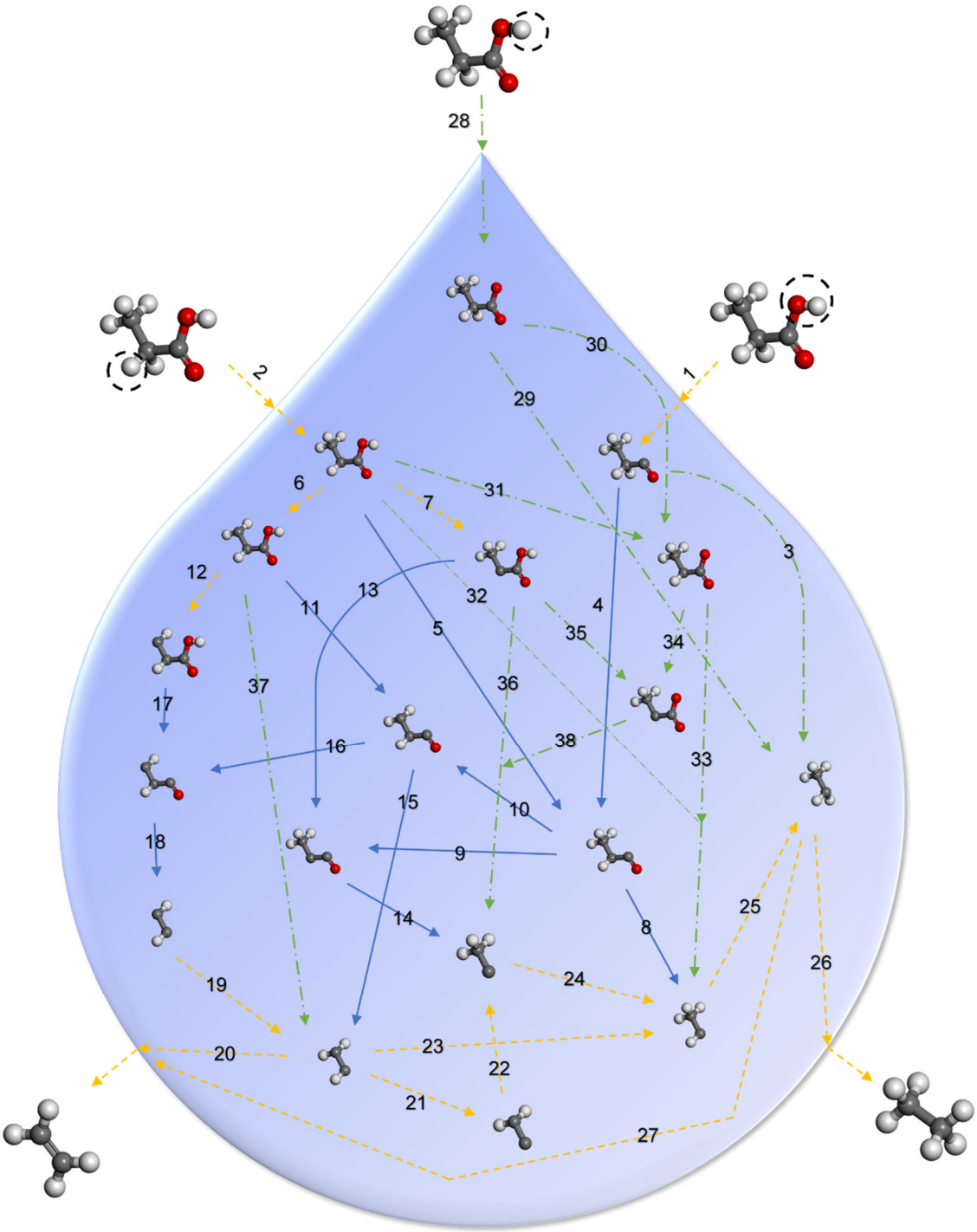

Figure 1. Reaction network for the HDO of PAC to ethane and ethylene. Blue solid arrows belong to the decarbonylation pathway, green dash-dotted arrows depict the decarboxylation pathway, and yellow dashed arrows show those steps that are in common between the decarboxylation and the decarbonylation mechanism. In addition, the number on each arrow illustrates the corresponding elementary reaction in Table 3, and the dashed circles show the corresponding cleavage of fluid phase propanoic acid.

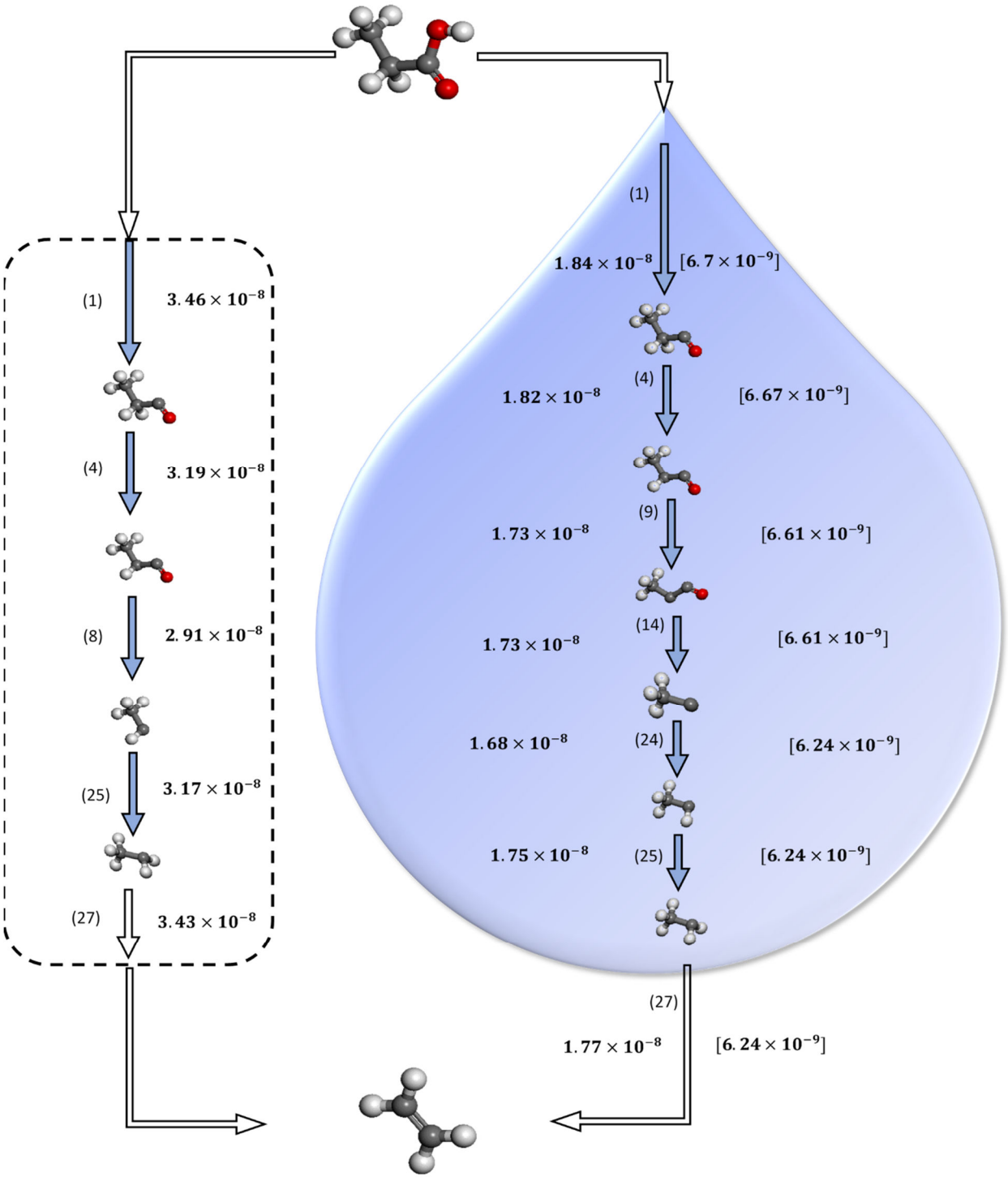

Figure 2. Schematic representation of TOF (s^{-1}), of various elementary reactions involved in the dominant pathways. The left dashed box illustrates the dominant pathway in the gas phase while the right blue drop displays the dominant pathways in the solvent environments. Numbers in parentheses () depict reaction step numbers. The numbers in square brackets [] in the right blue drop are the TOFs (s^{-1}) in liquid water and the numbers without square brackets are the TOFs (s^{-1}) in liquid 1,4-dioxane.

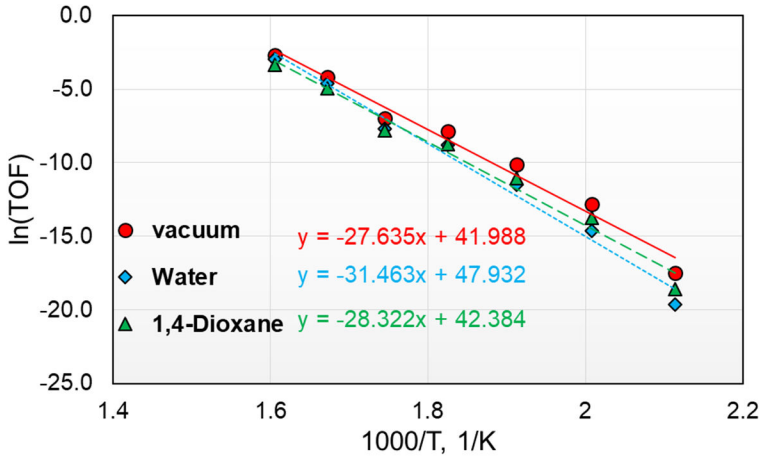

Figure 3. Apparent activation energy plot in the temperature range of 473 to 623 K in gas and condensed phase environments. The apparent activation barrier is 2.38 eV in the gas phase, 2.71 eV in liquid water, and 2.44 eV in liquid 1,4-dioxane.

1 **Table of Contents (TOC) Image:**

2